thesis for the degree of Licentiate of Engineering

# High-speed Optical Interconnects in harsh environments

M. Bilal Aziz


CHALMERS

Photonics Laboratory
Department of Microtechnology and Nanoscience (MC2)
Chalmers University of Technology
Göteborg, Sweden, 2024

Adaptive optical interconnects in data centers
M. Bilal Aziz


ISSN 1652-0769
Technical Report MC2-453

Photonics Laboratory
Department of Microtechnology and Nanoscience (MC2)
Chalmers University of Technology
SE–412 96 Göteborg
Sweden
Telephone: +46 (0)76–219 58 50

Printed in Sweden by
Reproservice
Chalmers Tekniska Högskola
Göteborg, Sweden, 2024

Adaptive optical interconnects in data centers
M. Bilal Aziz
Photonics Laboratory
Department of Microtechnology and Nanoscience (MC2)
Chalmers University of Technology

## Abstract

Advancements in AI, machine learning, AR/VR, IoT, and cloud computing, along with the anticipated arrival of 6G, are driving innovations like telepresence and autonomous machine communication. These technologies demand robust data center infrastructure to manage exponentially growing data traffic. The speed of data centers depends on their interconnects, and for short-reach connectivity, optical interconnects (OIs) with VCSELs are preferred due to their high speed, compact size, and energy efficiency. However, when tested with real-world data, these systems often experience additional receiver sensitivity penalties, which remain insufficiently addressed in prior studies. Additionally, while copackaging the transceivers which enhances system capacity, it subjects components to harsh environments, underscoring the need for advanced optical interconnects that maintain performance across wide temperature ranges. This thesis examines the operation of optical interconnects in real-world scenarios. A comprehensive study on Pseudo-Random Binary Sequences (PRBS) examines longer patterns that closely resemble real data, addressing additional receiver sensitivity penalties associated with longer sequences through a line coding technique. The study, conducted through simulations and experiments, uses a directly modulated VCSEL as the transmitter, a photodiode for direct detection, and multimode fiber for transmission. Results demonstrate 50 Gbps error-free transmission with a PRBS-31 sequence and 50-Gbps error-free transmission using PRBS-15 at 50°C when line coding is applied. The effectiveness of line coding increases under higher system stress, such as elevated data rates and temperatures. Additionally, improved VCSEL Quantum Well (QW) designs show robust performance across a broad temperature range, achieving 25-Gbps error-free transmission at 140°C. These findings are essential for advancing interconnect systems capable of handling real data in harsh environments.

**Keywords:** optical interconnect, fiber communication, vertical-cavity surface-emitting laser (VCSEL), High-Speed Data Transmission, Pseudo-Random Binary Sequence (PRBS), Line coding technique.

# Publications

This thesis is based on the work contained in the following papers:

[A] M. Bilal Aziz, Stavros Giannakopoulos, Alexander Grabowski, Peter Andrekson "Word Length Dependent Sensitivity Penalty in High Speed VCSEL-Based Optical Interconnects", *Photonics Technology Letters*, **36**, Issue: 19, 1181 - 1184, 2024.

[B] M. Bilal Aziz, Hans Daniel Kaimre, Peter Andrekson "High-Speed Transmission of 850 nm VCSEL Optical Interconnects Across Wide Temperatures", submitted to *Photonics Technology Letters*, 2024.

# Contents

# Acknowledgement

First, I would like to thank my supervisor, Professor Peter Andrekson, for giving me the opportunity to study towards a PhD and for all of the support and supervision along the way. I am grateful to my and examiner Professor Magnus Karlsson for valuable support and guidance. I also thank my co-supervisor Dr. Stavros Giannakopoulos for sharing helpful knowledge and insights.

I am thankful to all the wonderful and brilliant people in the Photonics laboratory that I thoroughly enjoy discussing and working with. I am grateful to Dr. Alexander Grabowski and Hans Kaimre for helping me out in the lab measurements. I would like to thank everyone at the VLSI and Electrical Engineering group at Chalmers for their cooperation and remarkable working ambience in the lab and office premises.

I would also like to acknowledge the Swedish Foundation for Strategic Research (SSF) through the Project HOT OPTICS under Grant CHI19-0004 for financing my research and providing opportunities to participate in network conference and workshops at the partner institutes and industries.

Last but not least, I would like to thank my parents and my wife Aiman Shaikh for their incredible support throughout the years.

# Acronyms

| | |
|---|---|
| AWGN | Additive White Gaussian Noise |
| AI | Artificial Intelligence |
| AR | Augmented Reality |
| BER | Bit Error Rate |
| CPO | Co-Packaged Optics |
| DAC | Digital-to-Analog Converter |
| DC | Direct Current, Data center |
| EMB | Effective Modal Bandwidth |
| FIR | Finite Impulse Response |
| FFT | Fast Fourier Transform |
| FEC | Forward Error Correction |
| FIR | Finite Impulse Response |
| FFE | Feed Forward Equalization |
| GbE | Gigabit Ethernet |
| GHz | Gigahertz |
| Gbps | Gigabit per second |
| HPC | High-Performance Computing |
| IC | Integrated Circuit |
| IoT | Internet of Things |
| LFSR | Linear Feedback Shift Register |
| LP | Linearly Polarized |
| MMF | Multimode Fiber |
| NRZ | Non-Return to Zero |
| OFL | Overfill Launch Bandwidth |
| OOK | On-Off Keying |
| PCB | Printed Circuit Board |
| PC | Personal Computer |
| PRBS | Pseudo-Random Binary Sequence |
| QW | Quantum Well |

| | |
|---|---|
| RF | Radio Frequency |
| RIN | Relative Intensity Noise |
| SNR | Signal-to-Noise Ratio |
| SMF | Single Mode Fiber |
| TIA | Transimpedance Amplifier |
| VCSEL | Vertical-Cavity Surface-Emitting Laser |
| VNA | Vector Network Analyzer |
| VR | Virtual Reality |

# Chapter 1

# Introduction

The rapid advancement of Artificial Intelligence (AI), 5G, and the anticipated 6G network is reshaping the digital landscape, enabling data-intensive applications such as autonomous vehicles, edge computing, augmented and virtual reality, the Internet of Things, and high-definition remote surgeries. With projected 6G speeds of up to 1 TeraByte per second [1], these technologies are creating unprecedented data demands, leading to a substantial increase in global data traffic, as shown in Fig. 1.1. This growth underscores the need for robust high-performance computing (HPC) systems in both large data centers (DC) and smaller processing units to meet escalating data requirements [2–5].

Efficient data transfer within HPC systems and DC depends on interconnects that link switches, computing units, and storage components. Initially, coaxial and copper cables met these needs but fell short as data volumes grew. Fiber optics, introduced in the 1990s, revolutionized data centers with high-speed, long-distance transmission, low latency, and immunity to electromagnetic interference. In modern data centers, optical interconnects connect units via transceivers on server panels, while electrical interconnects link ICs to these transceivers. To manage increasing data traffic more efficiently, co-packaged optics (CPO) can be employed, a technique that reduces dependence on electrical links and enhances the system's bandwidth and energy efficiency [6, 7].

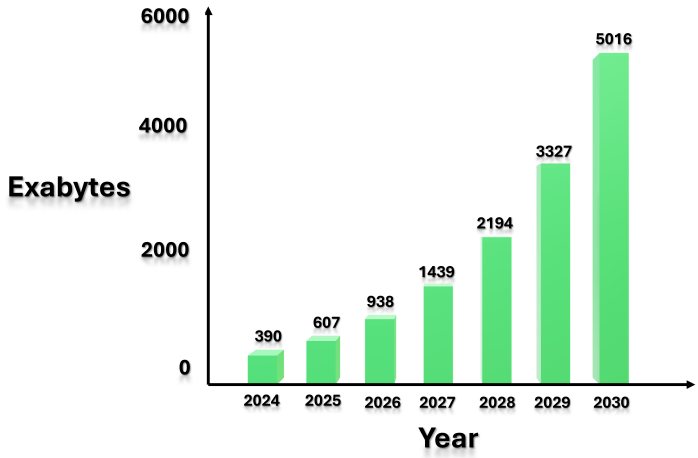


**Figure 1.1:** Global data traffic forecast by 2030 [8].

Figure 1.2 illustrates the Ethernet roadmap up to 2030, highlighting a significant increase in link speeds to meet the demands of advanced technologies and applications. Starting at 10 Mb/s in the 1980s, Ethernet advanced to the Gigabit Ethernet (GbE) range by the early 2000s. The following decade saw further growth with the development of 40 GbE and 100 GbE, driven by cloud computing, high-definition video streaming, and large-scale data centers. Ethernet speeds have since scaled to 200 GbE and 400 GbE, with future projections reaching 800 GbE and 1.6 TbE. By 2030, Ethernet speeds are expected to achieve 3.2 Terabit Ethernet (TbE) [9–11].

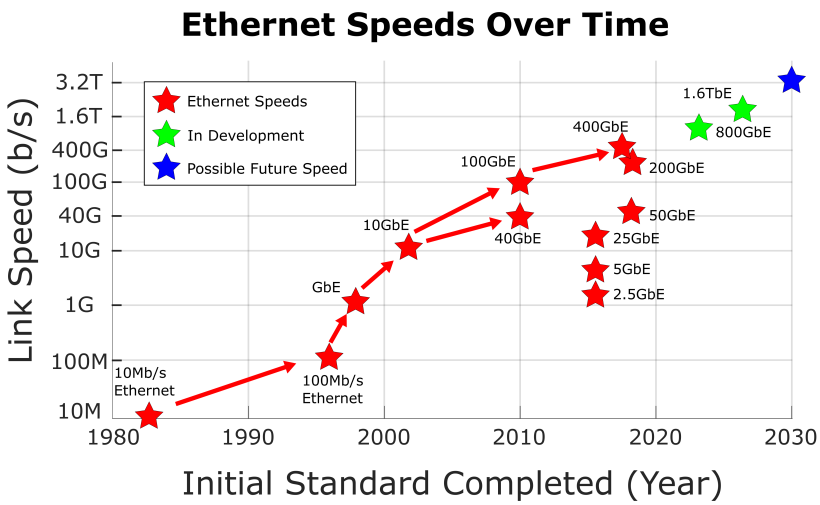


**Figure 1.2:** Evolution of Ethernet over the years [12].

## 1.1 Co-packaged optics

As data traffic increases exponentially, the need for faster data networks and device interfaces grows, which drives up energy consumption and heightens latency (delay in data transmission and processing within a network). Co-packaged optics (CPO)—the integration of silicon and optics on a single substrate as shown in Fig.1.3 — addresses these challenges by enabling low-latency, energy-efficient systems, essential for modern high-performance computing. Optical fibers transformed network infrastructure by enabling seamless connections between optical modules and ICs on PCBs. However, as network speeds push to 400 Gbps and beyond, bandwidth limitations arise, particularly in transmitting high-frequency signals from ICs centrally located on PCBs to front-panel modules. Here, CPO offers a critical solution by positioning optics closer to ICs, effectively supporting the continued evolution of high-speed networks [13,14].

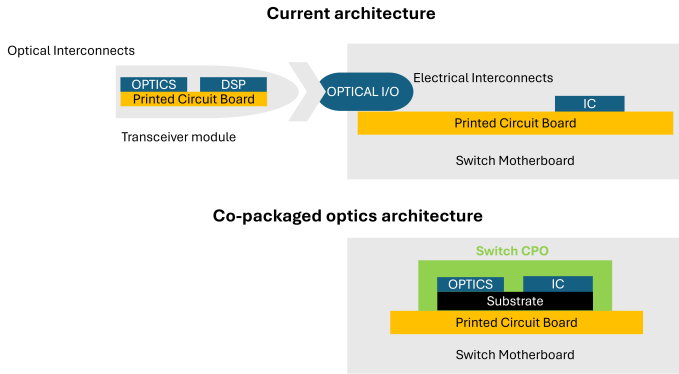


**Figure 1.3:** Block diagram comparing co-packaged optics with the traditional approach of using transceivers with digital signal processing (DSP) connected to integrated circuits (ICs) [15].

## 1.2 Objective and structure of the thesis

This work aims to enhance vertical-cavity surface-emitting laser (VCSEL)-based optical interconnects for high-speed and energy efficient operation with real-time, random data and over a wide temperature range. For simplicity and cost efficiency, intensity modulation and direct detection (IM/DD) with directly modulated lasers are employed. To simulate real-world data, lab testing typically uses pseudo-random binary sequences (PRBS). While these sequences are not entirely random, they approximate random data well; however, longer PRBS patterns, though more realistic, introduce significant receiver sensitivity penalties compared to shorter sequences.

Moreover, in densely packed data centers utilizing co-packaged optics, components like VCSELs are particularly affected by temperature fluctuations, impacting overall channel stability. Thus, developing robust optical interconnects that perform reliably across temperature variations is essential. In this thesis, the penalties of using longer PRBS sequences are analyzed and addressed and the system performance under extreme temperatures are enhanced by incorporating advanced quantum well (QW) VCSEL designs that demonstrate improved stability and efficiency.

The structure of this thesis is organized as follows. Chapter 2 covers the fundamentals of short-range optical links, discussing key components, impairments, and noise sources in these systems. Chapter 3 provides an

overview of VCSEL fundamentals and details of the VCSEL design which is important for the thesis. Chapter 4 introduces the principles of PRBS, which are essential for later investigations. Chapter 5 describes the experimental measurement techniques employed in these studies. Chapter 6 explores state-of-the-art advancements and future directions for this research. Finally, Chapter 7 summarizes the main contributions of the research work.

# Chapter 2

# Short-Reach Optical Interconnect System

This chapter presents the fundamentals of short-reach optical interconnect systems. It outlines the core components and provides a brief explanation of each. The topics are organized into three sections: transmitter, channel, and receiver. Additionally, the chapter discusses the different noise sources affecting the system.

## 2.1 Overview

Like any other communication system, an optical interconnect consists of three core parts: the transmitter, the channel, and the receiver. The transmitter's role is to encode information into bits and send it to the receiver via the communication channel.

The communication channel serves as the medium that carries the signal to the receiver. As with any physical channel, bandwidth is limited, and noise is introduced, impacting signal quality. Additionally, several types of distortions can affect the signal as it travels through the channel:

- **Attenuation:** A decrease in signal strength as it propagates through the channel, influenced by factors like distance, signal frequency, and the transmission medium.
- **Interference:** Degradation in signal quality caused by multiple signals overlapping or interfering. These signals can be from multiple sources or from the same source travelling in nearby channels.

- **Noise:** An unwanted signal component introduced during transmission. Noise sources include environmental factors, electronic devices, and thermal fluctuations, which can obscure the signal, complicating information retrieval.

- **Dispersion:** Broadening of the signal pulse as it propagates, resulting from different frequencies within the pulse traveling at varying speeds. This leads to pulse broadening, reducing signal amplitude and potentially interfering with neighboring signals in time.

On the receiver side, the main task of the circuitry is to recover the data sent by the transmitter as accurately as possible. The receiver first collects the signal from the channel and then passes it through a receiving filter. The signal is then sampled, converting it from a continuous to a discrete form, followed by a decision-making step to extract the transmitted information.

A communication channel is typically characterized by two fundamental properties: bandwidth and signal-to-noise ratio (SNR) at the receiver. The capacity of a noisy channel can be determined using the Claude Shannon expression [16, 17]:

$$C = \mathrm{BW}\ \log_2(1 + \mathrm{SNR}), \tag{2.1}$$

where, 'BW' denotes bandwidth, and this expression is valid for linear channels with Additive White Gaussian Noise (AWGN). The data rate achievable in any channel depends on three main factors: available bandwidth, the signal levels, and channel quality. The Shannon capacity defines the maximum bit rate, or the upper limit, for information that can be transmitted over a channel in bits per second.

Data-centers require numerous interconnects that are fast, cost-effective, and power-efficient, driving the need for simple, low-cost systems. This is achievable using VCSELs as the laser source, multimode fibers (MMF) as the transmission medium, and photodiodes for direct detection. These components are discussed in the following sections [18–20].

## 2.2 Directly-modulated lasers

Initially, LEDs were used in short-range communication systems due to their compact size and low cost. However, as data rate demands have

increased with modern applications, LEDs lack the necessary modulation bandwidth to meet these requirements. This shift in demand has directed attention toward directly-modulated lasers, which are preferred in data-center optical interconnects for their simplicity, power efficiency, and cost-effectiveness. Directly-modulated lasers also eliminate the need for bulky and expensive modulators within the system.

Despite these advantages, directly-modulated lasers are unsuitable for long-reach systems due to their large chirp (change in frequency with time). For optical interconnects, 850 nm has become the standard operating wavelength, making GaAs-based lasers crucial for these applications. Among directly-modulated lasers [21], the Vertical-Cavity Surface-Emitting Laser (VCSEL) is widely used and discussed in detail in previous sections.

## 2.3 Multimode fibers (MMF)

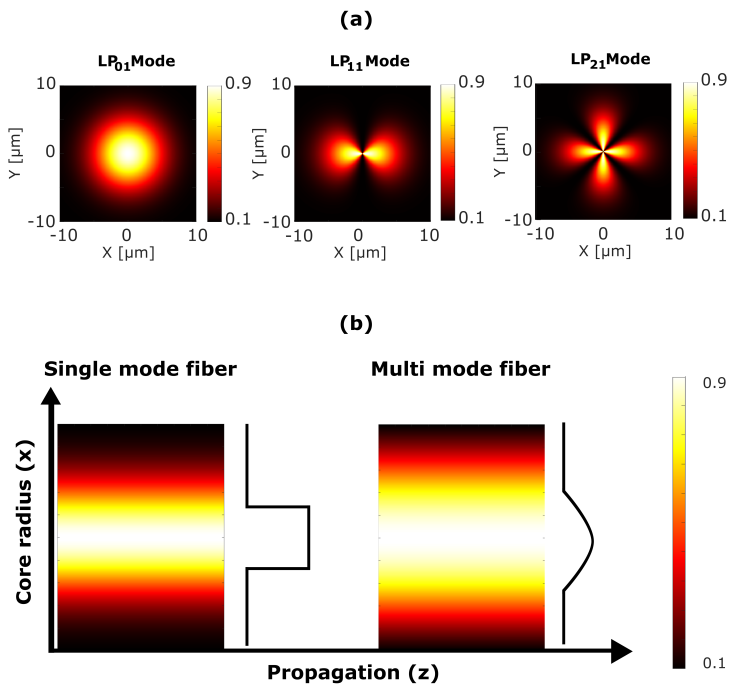


**Figure 2.1:** (a) Mode Field Distributions of LP 01, LP 11 and LP21 and (b) Intensity profiles of single mode and multimode fibers.

For short-range optical interconnects, multimode fibers (MMFs) play an essential role. Their larger core diameter enables easier coupling of light from the transmitter with straightforward alignment techniques, simplifying the system and reducing costs. However, MMFs have a higher cost per meter compared to single-mode fibers (SMFs) and are prone to intermodal dispersion. This dispersion causes pulse broadening, which limits the bandwidth-distance product. MMFs typically have a core diameter between 50 µm and 62.5 µm, whereas SMFs have a core diameter of around 9 µm. Light is guided through MMFs via total internal reflection, where the core's refractive index, $n_0$, is higher than that of the cladding, $n_1$. For the field to propagate as a mode in the waveguide, it must satisfy certain boundary conditions. Modes are solutions to the electromagnetic wave equation within the waveguide, which, in a weakly guiding dielectric waveguide $\Delta = (n_0 - n_1)/n_0 \ll 1$, can be reduced to a scalar wave equation:

$$\left(\nabla_t^2 + k_0^2 n^2(r) - \beta^2\right) E_t(r,\theta) = 0 \tag{2.2}$$

Here, $E_t$ represents the transverse electric field profile in cylindrical coordinates $(r, \theta)$ perpendicular to the fiber axis, $\beta$ is the propagation constant, $n(r)$ is the refractive index (assumed symmetric around the fiber axis for simplification), and $k_0$ is the wavenumber. Solving this equation provides linearly polarized modes (LP modes), which describe how light of different patterns travels within the fiber. These modes are denoted by $LP_{ab}$, with subscripts indicating each mode's specific intensity distribution across the fiber core, as illustrated in Fig. 2.1(a). For instance, $LP_{01}$ represents the fundamental mode, where the subscript '1' indicates no intensity variation radially outward from the center, and '0' denotes a single peak in the angular direction. SMFs support only this fundamental mode, while MMFs support the fundamental mode along with several higher-order modes. The mode intensity profile of the 2 fibers is shown in Fig. 2.1(b). The number of modes a fiber supports can be determined using the V parameter, which indicates whether the fiber operates in single-mode or multimode [22–24]:

$$V = \frac{2\pi a}{\lambda}\sqrt{n_1^2 - n_0^2} \tag{2.3}$$

where a is the core diameter, and $\lambda$ is the wavelength of light propagating through the fiber. For fibers with larger V values, the approximate number of modes can be calculated as [25]:

$$N_{\text{modes}} \approx \frac{V^2}{2} \tag{2.4}$$

## 2.4 Graded-index fibers

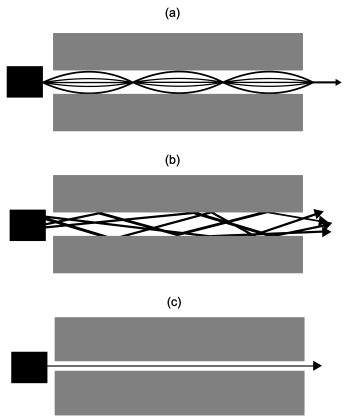


**Figure 2.2:** Ray optics representation of (a) Graded index (b) Step index and (c) Single mode fiber.

Different types of multimode fibers allow light to propagate in various mode profiles, each with distinct group velocities. For efficient communication, it is essential to use a mode configuration that reduces for intermodal dispersion, thereby increasing the system's transmission capacity. One such configuration features a high refractive index at the fiber axis, which gradually decreases with radial distance from the center, as shown in Fig. 2.2(a). This structure characterizes the cores of graded-index fibers, which follow a power law index profile. This profile mathematically describes the refractive index's radial variation as [26]:

$$n^2(r) = n_a^2 \left[1 - 2\left(\frac{r}{a}\right)^p \frac{n_a^2 - n_1^2}{2n_a^2}\right], \quad r \leq a \tag{2.5}$$

where $n_{\text{a}}$ is the refractive index at the fiber axis, $n_1$ is the refractive index at the core-cladding boundary, $r$ represents the radial distance from the center of the core, $a$ denotes the core radius, and $p$ is the profile exponent defining the shape of the refractive index profile. The mathematical analysis of multimode propagation is complex. To simplify, ray optics can approximate light propagation within fibers. Fig. 2.2 illustrates the

ray optics approximation for graded-index in Fig. 2.2(a), step-index in Fig. 2.2(b), and single-mode fibers in Fig. 2.2(c), offering an intuitive view of light behavior in different fiber configurations [27].

## 2.5 Types of MMF

In data communication, five standard types of fibers are commonly used for fiber communication: OM1, OM2, OM3, OM4, and OM5. OM1 and OM2 fibers have core diameters of either 50 µm or 62.5 µm, with a cladding diameter of 125 µm. In contrast, OM3, OM4, and OM5 fibers are standardized with a core diameter of 50 µm. These fibers are characterized by two key metrics: Overfilled Launch (OFL) bandwidth and Effective Modal Bandwidth (EMB). OFL bandwidth indicates the fiber's capacity when all modes are excited, reflecting the maximum data rate the fiber can support under full modal excitation. EMB, on the other hand, represents the data-carrying capacity when launch conditions are optimized to excite a selective number of modes, enhancing performance. Both metrics are expressed in MHz·km, representing the product of bandwidth and distance, meaning that as distance increases, available bandwidth decreases, and vice versa. A summary of the characteristics of these multimode fibers is provided in Fig. 2.3 [28, 29].

| Fiber type | OFL (MHz x Km) | EMB (MHz x km) |
|---|---|---|
| OM1 | 200 | Not specified |
| OM2 | 500 | Not specified |
| OM3 | 1500 | 2000 |
| OM4 | 3500 | 4700 |
| OM5 | Not specified | 4700 |

**Figure 2.3:** Representation of different fiber types and their bandwidths.

## 2.6 Signal reception

At the receiver end, a photodiode converts incoming optical power carrying information into a corresponding electrical signal. In short-reach interconnects, PIN photodiodes are commonly used due to their efficiency and simplicity. The photodiode's output current is directly proportional to the incident optical power, expressed as:

$$I = R_d P_{\text{in}} \tag{2.6}$$

where $P_{\text{in}}$ is the incident optical power, and $R_{\text{d}}$ is the photodiode responsivity expressed in amperes per watt (A/W). The responsitivity can be mathematically written as

$$R_d = \eta \frac{q}{h\nu} \tag{2.7}$$

where $\eta$ is the quantum efficiency, $q$ is the electric charge, $h$ is the planck's constant and $\upsilon$ is the incident light frequency. Typically, the photodiode's output current is weak, so an amplifier follows to boost signal strength. Some manufacturers integrate the amplifier within the same package as the photodiode, known as a Transimpedance Amplifier (TIA), producing a combined component called a photoreceiver. The TIA, converts photocurrent to voltage, making it more efficient for current-output devices like photodiodes. The signal is then processed by decision circuitry to extract the transmitted information. The photodiode's output signal contains both the transmitted information and noise. In direct detection systems, the electrical power is proportional to the square of the optical power (square-law detection). The ratio of signal to noise, or Signal-to-Noise Ratio (SNR), is given by:

$$\text{SNR} = \frac{\text{average signal power}}{\text{noise power}} = \frac{I^2}{\sigma^2} \tag{2.8}$$

where $R$ is the resistance, $I$ and $\sigma$ are the signal and noise powers, respectively. Both SNR and noise are measured in the electrical domain. Optical interconnect system performance is evaluated based on receiver sensitivity, which is the minimum optical power required to achieve a specific Bit Error Rate (BER). Such measurements are commonly referred to as BER measurements. In Intensity-Modulated Direct-Detection (IM/DD) systems, there are three primary noise sources: shot noise, thermal noise, and relative intensity noise (RIN) [2, 30].

- **Shot Noise:** This arises from the quantum nature of light and current. Even with continuous optical power on the photodiode, photon absorption and electron-hole generation occur at random intervals, resulting in discrete, random photocurrent pulses. The variance of shot noise is given by:

  $$\sigma_s^2 = 2qI\Delta f \tag{2.9}$$

  where $q$ is the elementary charge, $I$ is the average photocurrent, and $\Delta f$ is the receiver bandwidth. Shot noise increases with higher incident optical power.

- **Thermal Noise:** This is caused by the random movement of electrons due to kinetic energy at temperatures above absolute zero. This random movement generates unwanted current, known as thermal noise. The thermal noise variance is expressed as:

$$\sigma_t^2 = \frac{4k_B T \Delta f}{R_L} \tag{2.10}$$

  where $k_{\mathrm{B}}$ is the Boltzmann constant, $T$ is the temperature and $R_{\mathrm{L}}$ is the load resistance. In contrast with other noise sources, thermal noise is independent of the signal power and remains constant for a specific system.

- **Relative Intensity Noise (RIN):** This originates in the laser due to spontaneous emission, causing random-phase and frequency photons. In multimode lasers, RIN peaks at resonance and lower frequencies due to mode competition. The variance of RIN after the photodiode is:

$$\sigma_{\mathrm{RIN}}^2 = S_{\mathrm{RIN}} I^2 \Delta f \tag{2.11}$$

  where $S_{\mathrm{RIN}}$ is the RIN value (dB/Hz). RIN is signal-dependent, similar to shot noise, with noise variance proportional to the square of the photocurrent. Typically, thermal noise dominates, but at high received optical powers, RIN and shot noise may become more significant.

# Chapter 3

# Vertical-Cavity Surface-Emitting Lasers

This chapter introduces the fundamentals of the Vertical-Cavity Surface-Emitting Laser (VCSEL). It covers the basic architecture, key principles, and operational processes of the VCSEL. Additionally, it addresses the thermal characteristics of the device and their impact on performance.

## 3.1 Fundamentals

In lasers, three main radiative processes describe light amplification: absorption, spontaneous emission, and stimulated emission. In absorption, photons excite electrons to higher energy levels, while in spontaneous emission, electrons in high-energy states drop to lower levels, releasing photons. Stimulated emission—the principle behind lasing—occurs when an incident photon prompts an excited electron to emit an identical photon with the same frequency, direction, and polarization. This process is essential for coherent light amplification and underpins the lasing mechanism [31–33].

For lasing to occur, optical gain is necessary, achieved by creating population inversion through a pn-junction in semiconductor materials. When an external bias is applied, electrons accumulate in the conduction band and holes in the valence band, enabling optical gain through stimulated emission. This gain must surpass or equal system losses for lasing to continue, typically facilitated by mirrors forming a resonant cavity that allows certain photons to multiply through repeated interactions. As energy is introduced, the gain increases to a threshold level

where stimulated emission begins, transforming the VCSEL from a Light Emitting Diode (LED)-like state into a laser. Additional requirements for lasing include a source of external energy, an optical cavity, and photon emission to produce the final laser output. This relationship is quantified by the threshold gain, expressed as follows

$$g_{\text{th}} = \frac{1}{\Gamma}\left(\alpha_i + \alpha_m\right) = \frac{1}{\Gamma}\left(\alpha_i + \frac{1}{2L}\ln\left(\frac{1}{R_1 R_2}\right)\right), \tag{3.1}$$

where $\Gamma$ is the confinement factor, representing the overlap between the gain region and the optical field, $L$ denotes the cavity length, $\alpha_i$ and $\alpha_m$ are the internal losses and mirror losses respectively.

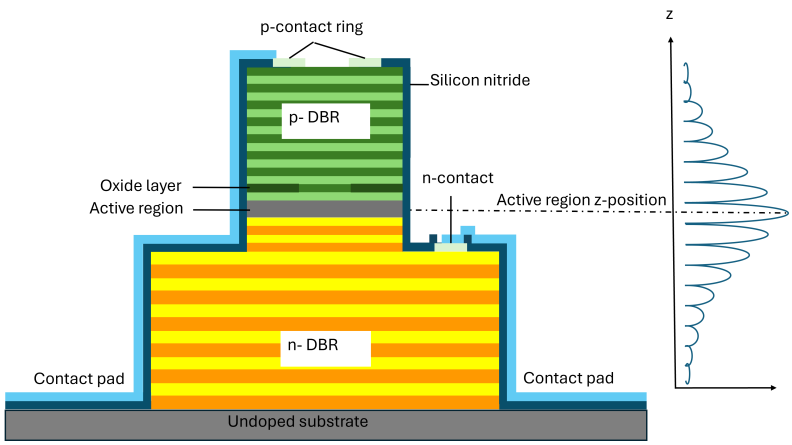


**Figure 3.1:** Cross-sectional view of the VCSEL with mode overlapping.

A second condition for laser operation is the phase condition, which states that not all wavelengths supported by the cavity will lase. Only those wavelengths that satisfy the phase requirement will amplify. Wavelengths that do not meet this condition interfere destructively and fail to amplify. On the other hand, wavelengths with the correct phase will remain in sync, resulting in constructive interference and amplification, leading to a high-intensity, stable laser output. The phase condition can be mathematically written as

$$\exp\left(-j\frac{2\pi}{\lambda_0}2Ln_{\text{eff}}\right) = 1, \tag{3.2}$$

where $n_{\text{eff}}$ is the effective refractive index of the cavity, and $\lambda_0$ is the lasing vacuum wavelength. The expression can be fulfilled when

$$\lambda_0 = \frac{2Ln_{\text{eff}}}{m}, \tag{3.3}$$

Where $m$ is a non-zero integer. The above expression shows that different values of $m$ allow the cavity to support multiple wavelengths. However, as illustrated in Fig. 3.1, most of the field fall outside the gain medium. In the case of VCSELs, which have a very short cavity length 'L', even fewer modes are supported, further limiting the number of wavelengths that can be amplified [34–37].

## 3.2 Basic Architecture and Concepts of VCSEL Technology

The VCSEL is a surface-emitting laser with its resonators aligned vertically. Its basic design consists of a bottom resonator, a cavity in the middle, and a top resonator. Light is typically emitted from the top resonator, though emission from the bottom is also common. A top-surface-emitting 850 nm GaAs VCSEL is discussed in this thesis.

Both resonators are usually distributed Bragg reflectors (DBRs) with very high reflectivity. The VCSEL architecture is designed with an undoped semiconductor serving as the active region, sandwiched between higher bandgap mirrors. Typically, the top mirror is p-doped and the bottom mirror is n-doped, forming a pn-junction that is forward biased to generate optical gain in the small active region at the center of the device. Electrical current is injected through the n-contact and p-contact using the gold contact pads on the top surface, allowing for easy probing.

When comparing surface emitting lasers with edge emitting ones, a key difference is the direction of resonators. The resonators are placed horizontally as comparison to the VCSEL where the resonators are placed vertically. Consequently, the emission from these lasers is from the edge rather than the surface. These horizontal resonators are created by cleaving the material. The vertical cavity allows VCSELs to be tested on the wafer during fabrication, unlike edge-emitting lasers, which cannot be wafer-tested during the manufacturing process. This advantage enables VCSELs to support mass production and offers cost efficiency. Additionally, their smaller size provides further benefits over edge-emitting lasers. Furthermore, as shown in Fig. 3.2, the VCSEL beam is circu-

lar in shape thanks to the symmetric design while the beam of the edge emitting laser is elliptical in nature which increases the need of expensive lenses to couple the light into the fiber. However, VCSELs with their smaller size are more susceptible to higher temperatures at lower current injections [38, 39].

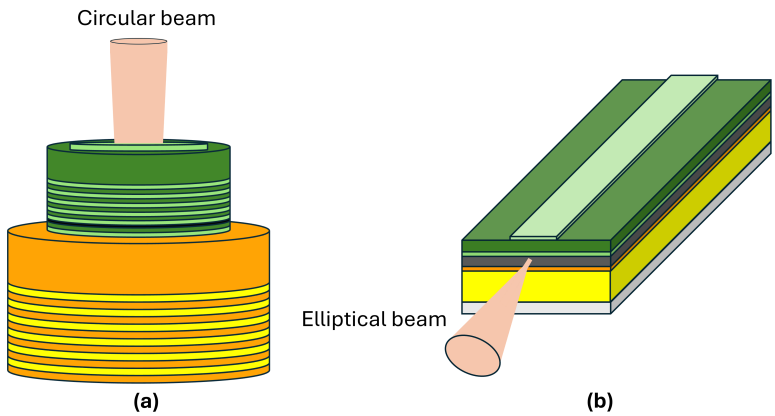


**Figure 3.2:** Schematics of (a) VCSEL and (b) Edge emitting laser.

## 3.3 Key Functional Aspects of VCSELs

The wavelength of a VCSEL is determined by the distance between the top and bottom DBR mirrors, each layer in the mirror is quarter-wavelength thick, and the thickness of the active region, also known as the cavity length. These DBR mirrors can be made from either the epitaxial material used in the active region or dielectric materials with alternating layers of high and low refractive index. In the case of GaAs-based VCSELs, the epitaxial mirrors are typically made from $Al_xGa_{1-x}As$, where the high and low refractive indices are achieved by varying the concentration of aluminum.

The cavity of the VCSEL contains QWs, which generate photons through stimulated emission when the optical wave overlaps them efficiently. These QWs are typically made of GaAs or InGaAs. InGaAs QWs, in particular, offer a strained structure that increases the differential resistance of the device, making them suitable for designing VCSELs

with high modulation bandwidth [40].

For high-speed VCSELs, 3-5 QWs are typically used. A higher number of QWs can spread the active region, resulting in inefficient overlap with the optical field. The QWs, which are usually 3-5 nm thick, must be carefully selected to ensure optimal overlap between the optical wave and the combined material gain of the QWs. The thickness of the cavity is typically a half-integer multiple of the wavelength (1/2-$\lambda$, 1-$\lambda$, 3/2-$\lambda$, etc.), but it is most commonly designed with a thickness of 1/2-$\lambda$ or 3/2-$\lambda$. Two different QW design VCSELs were analyzed and tested across wide temperatures in Paper B.

The QWs are positioned adjacent to one another in a higher bandgap separate confinement heterostructure (SCH) region, as shown in Fig. 3.3, with AlGaAs acting as barriers between them. These barriers create walls that confine the charge carriers, ensuring efficient light generation within the cavity.

In addition to longitudinal confinement in the vertical direction, transverse confinement of the charge carriers is also essential for efficient VCSEL operation. This is achieved using oxidized layers, which confine both the electrical and optical fields. By oxidizing AlGaAs with high aluminum content, an oxide aperture is formed within the VCSEL device. This layer is electrically insulating, which restricts the flow of electrical current to the aperture [41, 42].

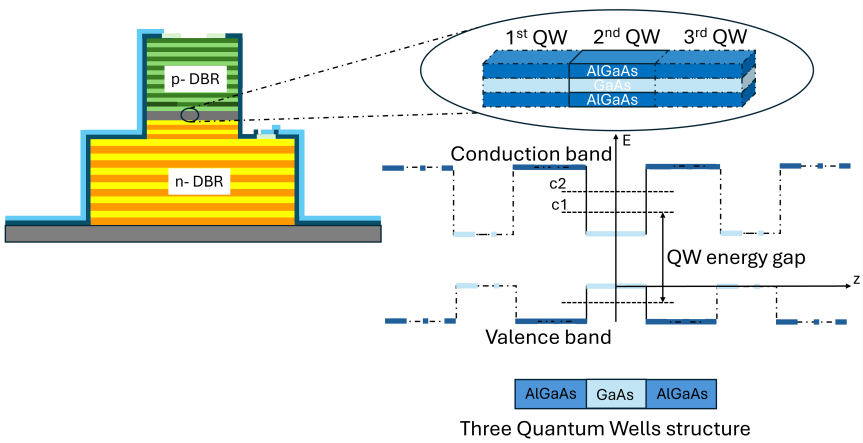


**Figure 3.3:** Representation of VCSEL QW structure.

Fig. 3.4 illustrates the modulation response of an 850-nm VCSEL

at different bias current levels. The bandwidth increases with higher bias currents until it reaches the resonance peak. Beyond this point, the bandwidth decreases sharply due to parasitic resistances and capacitances, which limit modulation at high frequencies. The 3-dB modulation bandwidth (indicated by the black dotted line) is the frequency where the bandwidth drops to 50% or 3 dB below its DC value [43, 44].

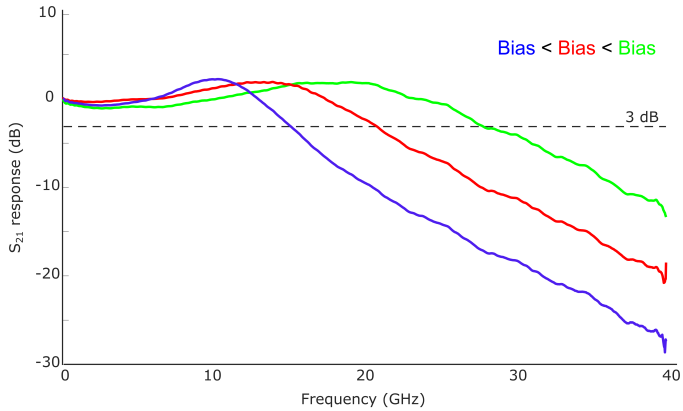


**Figure 3.4:** Representation of VCSEL QW structure.

## 3.4 Thermal characteristics of VCSEL

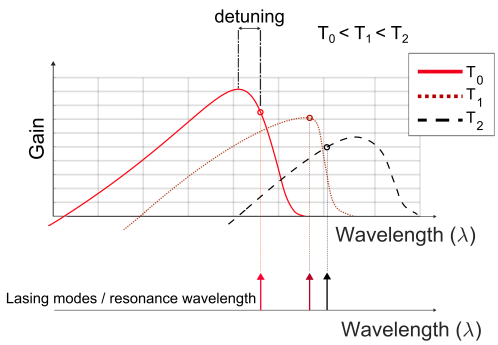


**Figure 3.5:** Schematics of VCSEL gain and modes shift as a function of temperature.

The resonance of a VCSEL is determined by the effective optical thickness of the cavity and the thickness of the DBRs, which provide sufficient reflectivity at the resonance wavelength. As the temperature increases, the gain spectrum shifts towards longer wavelengths (red shift), with the amount of shift depending on the composition and thickness of the QWs in the active region. The rate of this gain peak shift is approximately 0.32-0.33 nm/K [45].

However, due to Joule heating during current injection in the VCSEL, the materials within the device heat up, causing a change in the effective refractive index of the cavity. This alters the optical length of the cavity, resulting in a red shift of the resonance wavelength at a rate of approximately 0.06-0.09 nm/K [46]. This shift is influenced by multiple factors, including the composition of the VCSEL.

As shown in Fig. 3.5, the effect of temperature on both the gain spectrum and resonance wavelength can be observed. At room temperature, there is often a detuning, where the resonance wavelength does not perfectly match the gain peak. However, as temperature increases, the gain spectrum and resonance wavelength shift, eventually reaching an optimum operating temperature where the resonance wavelength aligns with the gain peak. Beyond this point, as temperature continues to rise, the gain peak drifts further, leading to a decrease in VCSEL performance [47–49].

# Chapter 4

# Pseudo-Random Binary Sequences

When testing systems in the laboratory, test engineers often use specific patterns designed to emulate real-time data found in actual systems. These patterns, known as Pseudo-Random Binary Sequences (PRBS), are widely used in testing high-speed serial interface devices. PRBS patterns help ensure that these devices perform reliably in real-world applications. While PRBS patterns have a continuous power distribution in the frequency domain, they repeat after a certain sequence length, meaning they are not fully random. The level of randomness depends on the sequence length: the longer the sequence, the more closely it resembles true random data.

PRBS patterns are not only used in digital functional tests but are also applied in mixed-signal tests, where they can be embedded within a modulation signal. In system testing, PRBS patterns are crucial, and understanding their generation is essential. Details on how these sequences are generated are discussed in the following section [50].

## 4.1 Linear-Feedback Shift Register (LFSR)

A Pseudo-Random Binary Sequence (PRBS) can be generated using various methods, with one common approach being the use of a Linear Feedback Shift Register (LFSR). An LFSR is a shift register made up of a series of flip-flops connected sequentially. It performs discrete operations where all bits in the sequence are shifted to the left, and the leftmost bit is shifted off (discarded). The vacant rightmost bit is then

filled with the result of multiple XOR operations between the bits taken from multiple positions in the shift register. The length of the generated Pseudo-Random Binary Sequence (PRBS) is determined by the number of shift registers in the Linear Feedback Shift Register (LFSR). The PRBS sequence is characterized by three essential parameters:

1. **Seed**: The initial sequence of bits used to initialize the register.
2. **Number of Bits**: Defines the maximum length of the generated sequence.
3. **Tap Position**: Specifies the bit position used in the XOR operation to generate new bits. If the tap position is not optimal, the generated sequence will not reach its maximum length, resulting in a shorter, more frequently repeating sequence.

These parameters collectively define the behavior and characteristics of the PRBS sequence generated by the LFSR [51].

## 4.2 PRBS generation

Fig. 4.1 illustrates the logic diagram of a 4-bit PRBS generator, which consists of 4 D-type flip-flops. A D-type flip-flop functions as an electronic memory element that retains its output state until a change in the input occurs, updating its output state on a rising clock pulse. The truth table for the D flip-flop is shown in Fig 4.2(a).

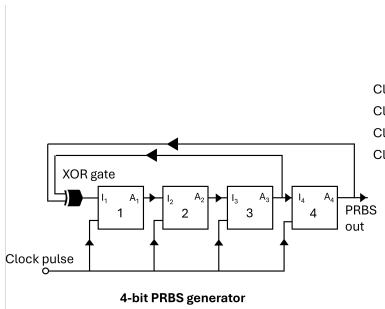


| | $A_1$ | $A_2$ | $A_3$ | $A_4$ |
|---|---|---|---|---|
| Seed value | 1 | 0 | 0 | 0 |
| Clock pulse 1 | 0 | 1 | 0 | 0 |
| Clock pulse 2 | 0 | 0 | 1 | 0 |
| Clock pulse 3 | 1 | 0 | 0 | 1 |
| Clock pulse 4 | 1 | 1 | 0 | 0 |
| | 0 | 1 | 1 | 0 |
| | 1 | 0 | 1 | 1 |
| | 0 | 1 | 0 | 1 |
| | 1 | 0 | 1 | 0 |
| | 1 | 1 | 0 | 1 |
| | 1 | 1 | 1 | 0 |
| | 1 | 1 | 1 | 1 |
| | 0 | 1 | 1 | 1 |
| | 0 | 0 | 1 | 1 |
| Clock pulse 14 | 0 | 0 | 0 | 1 |

**Figure 4.1:** Block diagram of D flip-flops constituting a LFSR.

| $I_1$ | Clock | $A_1$ |
|---|---|---|
| 0 | No rising edge | 1 |
| 0 | Rising edge | 0 |
| 1 | Rising edge | 1 |

(a)

| x | y | x⊕y |
|---|---|---|
| 0 | 0 | 0 |
| 0 | 1 | 1 |
| 1 | 0 | 1 |
| 1 | 1 | 0 |

(b)

**Figure 4.2:** Truth table of (a) D flip-flop and (b) XOR gate.

The PRBS sequence is generated by providing feedback from flip-flop 3 and flip-flop 4 to the input of the first flip-flop through an XOR gate. The truth table for the XOR gate is also shown in Fig 4.2(b). The outputs of $A_3$ and $A_4$ provide the input to $I_1$ via an XOR gate. The initial state for the flip-flops is set to 0 0 0 1, as starting with 0 0 0 0 would cause the shift register to get stuck, producing only zeros.

For each clock pulse cycle, the PRBS generator outputs a single PRBS bit (either 0 or 1). After 14 clock pulses, the PRBS generator has produced a sequence of 15 bits, which corresponds to $2^4$-1. This 4-bit LFSR can be mathematically represented by the polynomial $x_4 + x_3 + 1$, generating a PRBS sequence such as (0 0 0 1 0 0 1 1 0 1 0 1 1 1 1). Generally, if the system has m flip-flops, the maximum length of the sequence will be $2^m - 1$. Each PRBS sequence of $2^m - 1$ bits includes all possible combinations of m bits, excluding the all-zero state, as previously discussed. The -1 in the formula accounts for this missing state.

The data rate of the output PRBS is determined by the clock frequency supplied to the PRBS generator. Typically, PRBS generators operate at low clock frequencies. To achieve high-speed PRBS generation, multiplexing is applied. One key property of a PRBS sequence is that if it is shifted by half of its length and then combined (multiplexed) with its unshifted version, the resulting PRBS remains identical to the original sequence. This property allows high data rates to be achieved by efficiently multiplexing the PRBS streams, resulting in a faster PRBS output [52].

## 4.3 PRBS Bandwidth and Spectral analysis

In this section, we will focus on NRZ (Non-Return-to-Zero) sequences. As previously discussed, PRBS patterns are not fully random, as they repeat after a specific sequence length. This periodicity causes the power

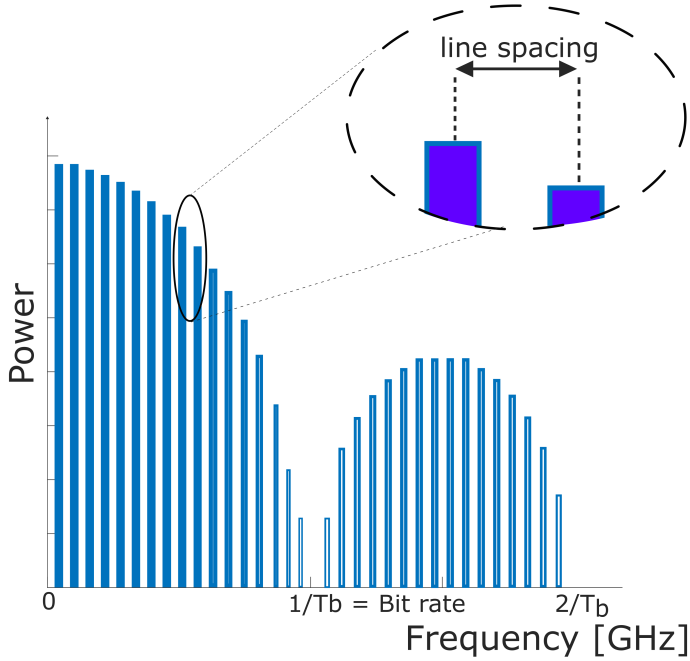


**Figure 4.3:** Frequency spectrum of a PRBS sequence.

spectrum of the PRBS to consist of discrete, equally spaced lines rather than a continuous spectrum. The distance between two adjacent lines is referred to as line spacing, as illustrated in Fig. 4.3. A longer sequence length results in a denser spectrum, meaning closer line spacing. These spectral lines are enveloped by a curve. In case of square shaped pulses, it can be mathematically approximated as follows.

$$\left(\frac{\sin f}{f}\right)^2 \quad \text{or} \quad \text{sinc}^2(f). \tag{4.1}$$

Here, $f$ represents the frequency. The longer the generated PRBS sequence, the closer its envelope approximates to a $sinc^2(f)$ function. This results in zero power at the clock frequency. The line spacing (also defines the sequence repetition rate) between spectral lines can be mathematically represented as

$$\text{line spacing} = \frac{\text{bit rate}}{2^m - 1} \tag{4.2}$$

Here, $2^m - 1$ denotes the sequence length, where $m$ is the number of

registers in the PRBS generator. This indicates that line spacing depends on both the bit rate and sequence length. Fig. 4.4 shows commonly used PRBS sequences and their corresponding line spacing when the bit rate is kept constant. From this, it is evident that a longer sequence length leads to a denser spectrum. Consequently, in testing, it stresses more frequencies within the system, similar to testing with continuous signals in a real environment. Fig. 4.5 illustrates the time-domain representation of a PRBS signal and its corresponding frequency-domain spectrum. In this example, a 4-bit LFSR generating a 15-bit sequence is shown.

| Pattern | Number of bits | Line spacing at 32 Gbps | Line spacing at 56 Gbps |
|---|---|---|---|
| $2^7$-1 | 127 | 252 MHz | 441 MHz |
| $2^9$-1 | 511 | 63 MHz | 110 MHz |
| $2^{11}$-1 | 2047 | 15.6 MHz | 27.4 MHz |
| $2^{15}$-1 | 32767 | 977 kHz | 1.7 MHz |
| $2^{20}$-1 | 1048575 | 30.5 kHz | 53.5 kHz |
| $2^{23}$-1 | 8388607 | 3.8 kHz | 6.7 kHz |
| $2^{31}$-1 | 2147483647 | 14.9 Hz | 26.1 Hz |

**Figure 4.4:** Table showing different PRBS and their corresponding line spacing.

The time-domain representation of this sequence is depicted in Fig. 4.5(a). Fig. 4.5(b) shows the Fast Fourier Transform (FFT) of this time-domain signal at a bit rate of 1 Gbps. The main lobe spans frequencies up to 1 GHz, which matches the bit rate of the signal. The signal's power is zero at 1 GHz ($1/\mathrm{T_{bit}}$) and again at multiples of this frequency, such as $2/\mathrm{T_{bit}}$, $3/\mathrm{T_{bit}}$, and so on. The number of spectral lines in the main lobe corresponds to the sequence length, which is 15 bits in this case. The side lobes also contain the same number of spectral lines, resulting in a total of 15 spectral lines in each lobe, including the DC component. Consequently, the line spacing in this case is

$$\text{line spacing} = \frac{1\,\text{Gbps}}{15} = 66.66\,\text{MHz} \tag{4.3}$$

When recovering a PRBS signal using a filter (Inverse Fast Fourier Transform) with a specified cutoff frequency, the cutoff frequency will determine the efficiency of the signal recovery. For instance, if a narrow bandwidth filter with a cutoff frequency of 1 GHz is used, capturing only the main lobe and discarding the side lobes, the resulting signal will be a rough approximation, as shown in Fig. 4.5(c). As the filter bandwidth increases, more frequency components are included, improv-

ing the quality of the recovered signal and allowing it to more closely resemble the original, as illustrated in Fig. 4.5(d) and Fig. 4.5(e). If the bit rate is increased tenfold to 10 Gbps, the corresponding results are displayed in Fig. 4.5(f),Fig. 4.5(g), Fig. 4.5(h), and Fig. 4.5(i). In Figures Fig. 4.5(g) and Fig. 4.5(h), where the filter bandwidth is insufficient to cover the full main lobe of the signal, a significant loss of high-frequency components prevents effective signal recovery. Conversely, if the filter bandwidth is too high, additional system noise may be incorporated, degrading the signal-to-noise ratio (SNR) [53, 54]. This concept is critical in understanding additional penalties associated with longer sequences, like PRBS-31. In a bandwidth-limited system, PRBS-31 loses more high-frequency components than PRBS-7 (Similar can be understood for the low frequency cut-off point of the system), as it has a denser spectral line distribution. This loss impacts the PRBS-31 waveform more than PRBS-7, degrading its shape. Furthermore, PRBS-31's denser spectrum places greater stress on the system, exposing it to impairments within the system response that may not be as prominent in the less dense spectrum of PRBS-7.

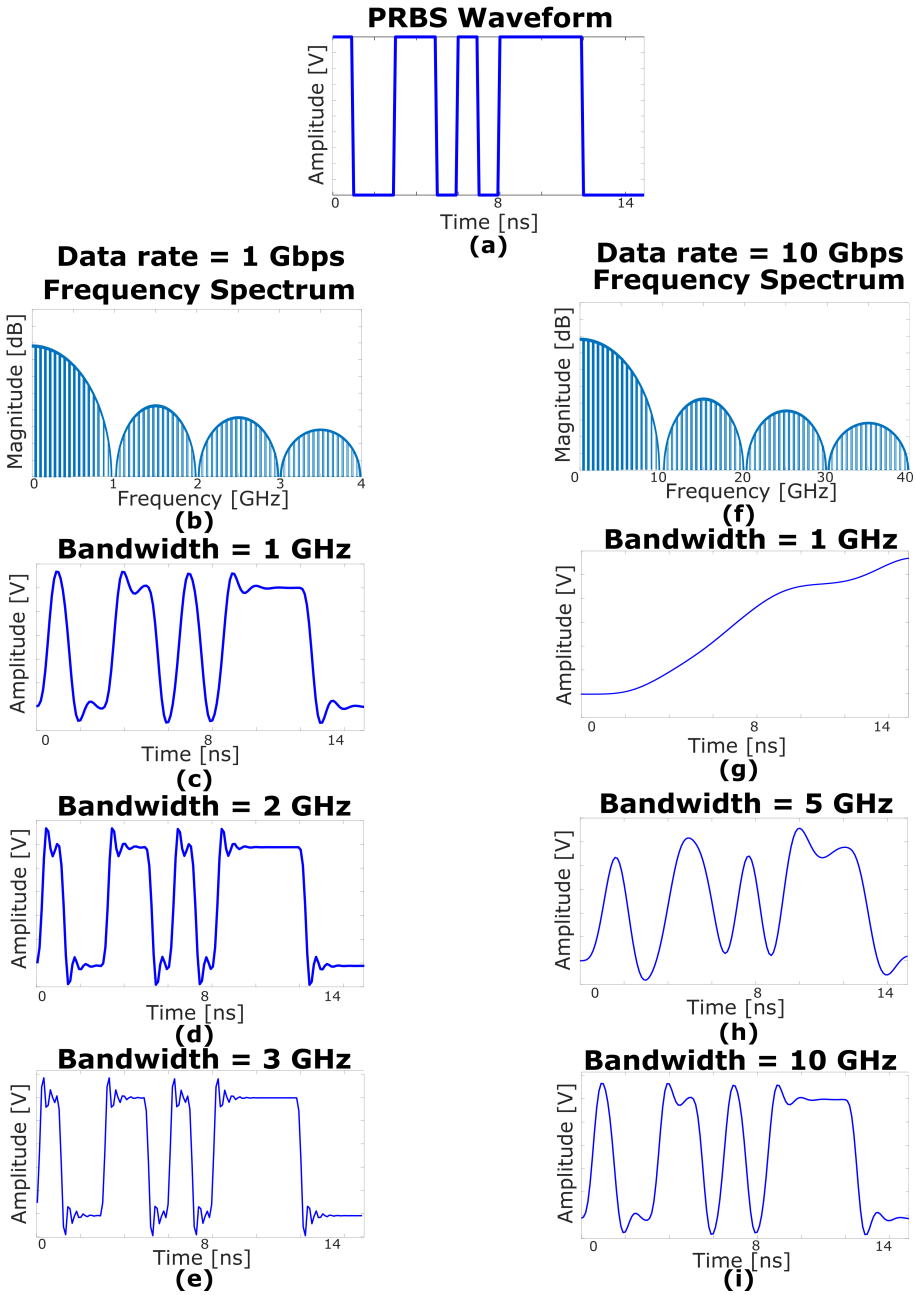


**Figure 4.5:** 4-bit PRBS signal representation: (a-e) Time and frequency domain at 1 Gbps, with reconstructions at 1, 2, and 3 GHz bandwidth; (f-i) Frequency domain at 10 Gbps, with reconstructions at 1, 5, and 10 GHz bandwidth

# Chapter 5

# Measurements

This section discusses small-signal and large-signal measurements of VCSELs, along with techniques to enhance link performance. Among small-signal measurements, one of the most critical is the IPV (or LIV) measurement as shown in Fig. 5.1, where 'I' represents the current, 'P' is the corresponding optical power, and 'V' is the voltage drop across the VCSEL. Another essential small-signal measurement is bandwidth, as it determines the device's frequency response.

For large-signal measurements, eye diagram and bit error rate (BER) analyses are among the most commonly used tests. These provide insights into VCSEL performance under high-speed modulation, assessing its viability for optical communication systems. Additionally, increasing link bandwidth directly improves throughput. Techniques like pre-emphasis and forward error correction are also discussed in this thesis as methods to enhance link performance.

## 5.1 Small-signal measurements

In IPV measurements, a sweep of bias currents is applied to the VCSEL, and the corresponding voltage drop at each current is recorded using a voltmeter. Output power is measured using a wide-area photodiode, where the generated current interacts with a load resistor to produce a measurable voltage that can be converted into power. A larger photodiode area captures more light, but a more accurate measurement involves using an integrating sphere, which provides isotropic light scattering for higher accuracy. Several parameters are derived from the IPV measurements, including the threshold current, which marks the point where

the VCSEL begins lasing. Lower threshold current indicates less cavity losses, while higher values suggest increased internal losses. Slope efficiency, measured in watts per ampere, reveals the VCSEL's efficiency in converting current to optical output. The roll-over current indicates the thermal characteristics of the VCSEL, where excessive bias leads to overheating and decreased output. Differential resistance, represented by the IV curve slope, shows the voltage change with current variations and affects heat generation and power loss; lower differential resistance is preferred for high-speed communication due to faster switching capabilities. A comparison of two VCSEL designs offering different differential resistance across temperatures in done in Paper B.

For wide temperature IPV measurements, the VCSEL is held in a probe station with vacuum and temperature control. The bandwidth of the VCSEL is measured using a Vector Network Analyzer (VNA), which sends small signals over a range of frequencies. The VCSEL's output is coupled into an optical fiber connected to a photodiode, with the resulting signal analyzed by the VNA to determine the S21 parameter, which reveals the VCSEL's bandwidth and response across the frequency spectrum [55–57].

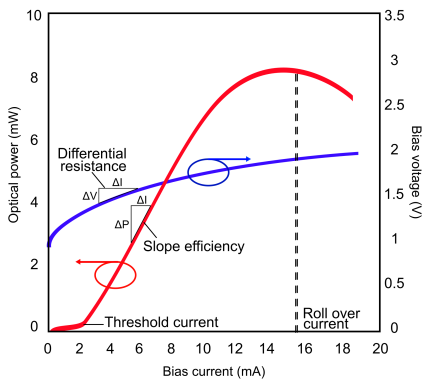


**Figure 5.1:** IPV curve of a VCSEL.

## 5.2 Large-signal measurements

Large-signal measurements evaluate system performance under high-power, real-world signals, offering insights into actual working conditions. A key test is the BER measurement, which assesses system performance

by analyzing transmission errors across various operating conditions. In Paper A, BER is used to characterize performance with different PRBS, and in Paper B, it evaluates performance over a wide temperature range. BER measurements are discussed in the next section. The eye diagram is another essential tool for visualizing signal quality over time, often complemented by jitter analysis to assess signal timing accuracy. Energy efficiency measurements are also performed to evaluate power consumption under varying conditions, while temperature-based tests, explored in Paper B, observe system behavior across a wide temperature range.

The experimental setup for large-signal measurements is shown in Fig. 1 in Paper B. A clock source synchronizes the transmitted and received patterns. To simulate real data in the lab, pseudo-random binary sequences (PRBS) are generated by a bit pattern generator (SHF 12103a), with the clock source also feeding an error analyzer (SHF 11100b) to ensure synchronization. This alignment helps in accurately identifying the transmitted pattern. The transmitted pattern is attenuated to keep the signal within the amplifier's linear region, which is operated at its 1 dB compression point, as illustrated in Fig. 5.2. The RF signal is then sent through a bias tee that combines the DC bias with the RF signal before feeding it to the VCSEL via the n and p contacts [31].

The 850 nm VCSEL output is coupled into an OM4 graded-index multimode fiber (MMF) using a lensed tip, passing through a variable optical attenuator (VOA) to simulate propagation through a link. For example, a 3 dB attenuation corresponds to approximately 1 km in OM4 MMF at 850 nm. The attenuated signal is received by a photoreceiver, which converts the optical signal back to an electrical signal, then sent to the error analyzer. Here, it is compared with the transmitted pattern to calculate bit errors. Accurate error calculations require optimizing parameters such as VCSEL bias current, driving voltage swing, horizontal delay, and vertical threshold in the error analyzer. This careful alignment ensures reliable error detection and a comprehensive evaluation of system performance [58].

### 5.2.1 Bit error rate measurements

#### Overview

Modern digital communication systems have introduced the need for end-to-end performance measurements in radio engineering. BER is

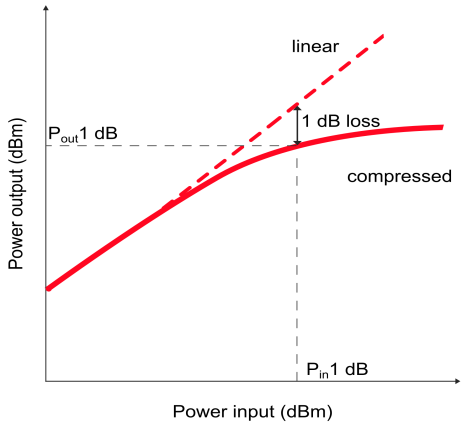


**Figure 5.2:** 1 dB compression point of an amplifier.

commonly used to quantify this performance, providing a measure of the system's reliability from input to output. This metric captures the accuracy of the entire system, encompassing the transmitter, receiver, and the signal path between them. BER can be simply expressed as

$$\text{BER} = \frac{\text{Total bit errors}}{\text{Total Number of Bits}} \tag{5.1}$$

With a strong signal and a less noisy transmission path, the BER is typically negligible. However, it becomes critical to manage when maintaining sufficient signal-to-noise ratio is challenging due to imperfections in transmission. These imperfections may arise from electronic components, such as amplifiers, filters, mixers, and converters, as well as from the channel, which can be a radio path or an optical fiber. For simplicity, it is assumed that the system is dominated by thermal noise with variance $\sigma$. Other noise sources, such as RIN and shot noise, are discussed in the previous sections. For a RIN below $-145\,\text{dBm/Hz}$ and received optical power below $0\,\text{dBm}$, the penalty introduced to the receiver sensitivity by these sources is negligible. In a direct detection system, the electrical current $I$ is proportional to the optical signal power $P$ through the photodiode responsivity $R_{pd}$, as described in section 2.6. For OOK, the BER at the receiver can be mathematically expressed as:

$$\text{BER} = \frac{1}{4}\left[\text{erfc}\left(\frac{I_1 - I_{\text{th}}}{\sigma\sqrt{2}}\right) + \text{erfc}\left(\frac{I_{\text{th}} - I_0}{\sigma\sqrt{2}}\right)\right], \tag{5.2}$$

where $I_0$, $I_1$, and $I_{\text{th}}$ represent the currents corresponding to bit '0', bit '1', and the decision threshold, respectively. Similarly, $P_0$ and $P_1$ are the optical power levels corresponding to bit '0' and bit '1'.

The optical modulation amplitude (OMA) can be expressed as:

$$\text{OMA} = P_1 - P_0.$$

If the decision threshold is placed in the middle of levels 0 and 1, then Equation (5.2) can be simplified to:

$$\text{BER} = \frac{1}{2}\,\text{erfc}\left(\frac{R_{PD}\,\text{OMA}}{\sigma\,2\sqrt{2}}\right), \tag{5.3}$$

where $R_{\text{pd}}$ is the photodiode responsivity, which depends on the wavelength and the receiver. The noise variance $\sigma$ is influenced by the system bandwidth (and consequently the bit rate), temperature, noise figure, and load resistance. Although the concept of measuring BER is straightforward—transmit a data stream through the system and compare the output to the input—implementing it, is complex. Ideally, a BER measurement assumes an infinitely long data transmission as a random process, but this is impractical. Instead, pseudorandom binary sequences (PRBS) are used to approximate randomness. PRBS provides a repeatable, deterministic pattern, enabling quick and accurate BER measurements. PRBS are discussed in detail in section 4. To avoid the high costs and time required to test with fully installed system transmission lines, we use a variable optical attenuator. This attenuator intentionally degrades the signal and its SNR, simulating the effects of signal loss over distance, which allows for efficient BER performance testing [59].

### Factors affecting BER of the system

Noise is a primary factor affecting BER performance, as it is inherently random and defined statistically. Circuit noise is typically characterized by a Gaussian probability density function. Quantization errors also impact BER performance by introducing inaccuracies or ambiguities in the reconstruction of the digital waveform. These errors are defined by a probability function that estimates the likelihood of transition or edge detection errors. They largely depend on the precision of digital-to-analog and analog-to-digital conversion processes, which are influenced by the number of bits used in these conversions. Additionally, the accuracy of analog modulation/demodulation and the effects of filtering

on signal and noise bandwidth further affect quantization errors. Reducing noise power can be achieved by lowering the bandwidth, but this is constrained by the Nyquist criterion, which dictates the bandwidth needed to transmit the desired bit rate. Increasing the energy per bit by raising transmission power is another option, though this reduces the energy efficiency of the system. Alternatively, lowering the bit rate also increases the energy per bit, but it reduces overall capacity. Ultimately, optimizing the system requires balancing these factors or by introducing some advanced signal processing techniques which are discussed in the next section.

When high BER reduces a system's reliability, several solutions can be explored. The troubleshooting process begins by identifying the source of errors—whether they are caused by circuitry or transmission path issues. Decisions on corrective actions consider both effectiveness and cost. Options may include hardware improvements, modifications to the transmission environment, or selecting an alternative modulation format. In some cases, software-based error correction can be applied, a method used extensively in terrestrial and satellite communications. While these techniques reduce BER, they often come at the expense of lower data throughput and adding complexity [60, 61].

### 5.2.2 Signal processing techniques

Link bandwidth is essential for system capacity, and pre-emphasis enhances it by reshaping pulses at the transmitter, amplifying high-frequency components while reducing lower ones. This technique, often implemented with a finite impulse response filter, optimizes signal frequency response, improving performance beyond channel limitations [62]. Forward error correction (FEC) improves communication reliability by adding redundancy bits to correct errors in noisy channels without retransmission. Although it introduces data overhead and complexity, effective FEC codes minimize redundancy while significantly enhancing error correction. [63]. Line coding is a signal processing technique that converts binary data into a format suitable for transmission, ensuring properties like synchronization, DC balance, and error detection. This method aids in maintaining signal integrity, minimizing degradation and interference, and optimizing bandwidth for higher data rates. Additionally, certain line coding schemes support error identification and correction, enhancing transmission reliability and efficiency [64]. A similar line coding technique for error correction is explored in Paper A.

# Chapter 6

# State of the art and Future work

This chapter presents an overview of recent advancements in the field, highlighting key research in the data communication industry, with a focus on developments involving 850 nm VCSEL technology. It also explores future research directions and prospects, identifying potential areas for further improvement in this domain.

## 6.1 Outlook of the technology

Significant advancements have recently been made in the field of short-reach optical interconnects, as Vertical-Cavity Surface-Emitting Lasers (VCSELs) have seen substantial progress. VCSELs are now widely used in consumer electronics and have attracted strong interest from the datacom and telecommunications industries. Global efforts are underway to enhance VCSEL-based optical interconnect systems to meet the high demands of future Ethernet standards of 800 (Gigabit Ethernet) GbE and 1.6 (Terabit Ethernet) TbE. [65]

Since the invention of the VCSEL by Iga's group in 1978 [66,67] and the successful demonstration of room-temperature operation in 1988 [68], extensive research has expanded the capabilities of short-range VCSEL interconnects.

### 6.1.1 Datacom

The high modulation bandwidth of VCSELs makes them ideal for active optical cables and transceivers. In 2002, IEEE introduced the P802.3ae standard for 10 GbE [69]. In 2015, IEEE standardized the 100GBASE-SR4 (IEEE P802.3bm), employing four 25 GbE VCSEL lanes to support 100 GbE applications [70]. In 2017, IEEE P802.3bs introduced 400GBASE-SR16, which utilizes 16 lanes of 25 GbE VCSELs to enable 400 GbE Ethernet links [71].

By 2020, lane data rates doubled to 50 Gb/s under IEEE P802.3cm 400GBASE-SR8, further increasing system capacity [72]. Recently, electrical and optical single-lane interconnects at 50 Gb/s and 56 Gb/s were standardized by IEEE 802.3bs and OIF CEI-56G-VSR. Additionally, CEI-112G-VSR standards now support single-lane 100 Gb/s connections for chip-to-module applications [73].

### 6.1.2 850 nm VCSEL transmissions

In 2001, a VCSEL with an integrated SiGe driver demonstrated a 15.4 GHz modulation response, achieving 20 Gb/s on-off keying (OOK) over 2 km [74]. In 2010, a record 23 GHz modulation bandwidth was reported by Larsson's group at Chalmers University of Technology and Bimberg's group at TU Berlin [75,76]. This enabled back-to-back (BTB) error-free transmission at 40 Gb/s without forward error correction (FEC) [77]. In 2013, Larsson's group demonstrated a VCSEL with a modulation bandwidth of up to 28 GHz, capable of error-free transmission at 47 Gb/s [78]. That same year, P. Westbergh et al. achieved 57 Gb/s error-free BTB transmission using an 850 nm VCSEL [78]. Also in 2013, Moser et al. developed energy-efficient VCSELs with a power dissipation of just 56 fJ/bit [79]. In 2015, Larsson's group set a record with a 30 GHz VCSEL operating at a relatively low bias current [80]. Later that year, Kuchta et al. achieved 71 Gb/s error-free NRZ transmission with an 850 nm VCSEL using two-tap feed-forward equalization [81]. In 2019, Huang et al. demonstrated BTB error-free transmission at 54 Gb/s with a 4.23 µm aperture size VCSEL device [82]. Most recently, in October 2021, Yang et al. presented a high-speed VCSEL with a record bandwidth of 32.4 GHz [83].

### 6.1.3 850 nm VCSEL temperature performance

In 2016, C. Y. Wang et al. demonstrated back-to-back (BTB) error-free NRZ transmission up to 85°C using a 29 GHz VCSEL [84]. In 2018, Hsiao-Lun Wang et al. achieved error-free transmission at 43 Gb/s at 75°C and 42 Gb/s at 85°C with a 25 GHz VCSEL [85]. In 2019, Hsiao-Lun Wang et al. demonstrated error-free transmission at 50 Gb/s at room temperature using a 30 GHz VCSEL, along with error-free results of 44 Gb/s at 85°C, 36 Gb/s at 100°C, and 30 Gb/s at 115°C [86], all achieved without equalization or forward error correction (FEC). In the same year, N. Ledentsov Jr. demonstrated 25 Gb/s transmission at 150°C using an 850 nm quantum dot VCSEL [87]. In 2020, Ledentsov et al. further advanced this work, achieving 25 Gb/s transmission at 180°C with an 850 nm quantum dot VCSEL [88].

## 6.2 Future work and Research goals

VCSEL-based short-reach optical interconnects have made significant progress, advancing research in optoelectronics, fiber optics, and electronics. Recent developments in 5G technology and the approaching 6G era suggest that this technology will continue evolving as more advanced data centers are built to meet growing demands.

This thesis demonstrates areas where VCSEL-based optical interconnects can further develop. Notably, there remains untapped potential in 850 nm VCSEL interconnects, as explored in Paper A. In this study, the interconnects were enhanced to operate in real-time systems using longer PRBS sequences, which better simulate real-world data. The impairments caused by longer sequences were analyzed and addressed through both simulations and experimental results. This research aligns with advances from industry leaders like NVIDIA, who are developing methods to improve system performance with long PRBS sequences, thus addressing potential system issues. Future work on higher-order modulation formats and performance at elevated temperatures holds promise for continued advancement.

While much research has focused on optimizing VCSEL-based interconnects, there is limited published work on high-speed large-signal VCSEL transmissions across a broad temperature range. This range is critical for applications in the defense, datacom, and automotive industries, as well as in radar systems requiring temperature tolerance. Paper B addresses these needs, demonstrating transmission over a wide temper-

ature range and comparing two distinct VCSEL designs. This research will support the development of complete optical transceivers capable of operating across a wide temperature spectrum.

Future work will focus on enhancing optical interconnects under harsh operating conditions. The integration of high-order modulation formats, advanced FEC, and equalization techniques will be key to pushing system performance further. Additionally, incorporating machine learning into future systems could provide adaptability to varying operational conditions.

# Chapter 7

# Summary of papers

Two papers are included in the thesis. Paper A deals with enhancing the existing optical interconnects systems along with analyzing and improving their performance with real time data. Paper B deals with the system performance across wide temperature range. A summary of them is presented below.

## Paper A

**Word Length Dependent Sensitivity Penalty in High Speed VCSEL-Based Optical Interconnects**,
*Photonics Technology Letters*, Volume: 36, Issue: 19, 1181 - 1184, DOI: 10.1109/LPT.2024.3451141, 2024.

In this paper, the challenge of receiver sensitivity degradation in optical links driven by long pseudo-random bit sequences—a common issue generally linked to imperfect low-frequency responses in the system were analyzed and addressed. The focus was on vertical-cavity surface emitting lasers (VCSELs) and how their high-frequency dynamics interact with symbol rates that exceed their bandwidth. It was found that certain short bit sequences within these longer streams were largely responsible for increasing the power budget penalty. By modifying these specific sequences, a successful mitigation of these issues was made possible, enabling error-free transmission at high data rates of up to 56 Gbps and elevated temperatures using 850 nm VCSELs without the need for equalization. This addresses a previously unsolved problem, enhancing the efficiency and reliability of high-speed optical

interconnects.

**My contributions:** I conducted both the measurements and simulations with support from co-authors.

## Paper B

**High-Speed Transmission of 850 nm VCSEL Optical Interconnects Across Wide Temperatures**,
*Submitted*, 2024.

This paper presents advancements in optical interconnects using two different designs of high-performance 850-nm multi-mode VCSELs that are analyzed and tested across extreme temperature ranges. As transceiver proximity to integrated circuits increases in high-density setups, maintaining performance under thermal stress becomes critical. This study demonstrates record data rates, achieving 40 Gb/s at 115°C, 34 Gb/s at 125°C, and 25 Gb/s at 140°C without equalization or forward error correction. These results mark a significant improvement over previous benchmarks, setting new standards for VCSEL technology in optical interconnects by enabling high-speed, error-free transmission across challenging environmental conditions.

**My contributions:** I conducted the small signal and large signal measurements across wide temperatures.

# References


[1] P. A. J. (2021) What is 6G Technology, How Fast Will it be, and When is it Rolling Out? Accessed: 2024-11-04.

[2] L. Pavesi and G. Guillot, "Optical interconnects," *Springer series in optical sciences*, vol. 119, 2006.

[3] S. Aleksic, "The future of optical interconnects for data centers: A review of technology trends," in *2017 14th International Conference on Telecommunications (ConTEL)*. IEEE, 2017, pp. 41–46.

[4] S. Rumley, M. Bahadori, R. Polster, S. D. Hammond, D. M. Calhoun, K. Wen, A. Rodrigues, and K. Bergman, "Optical interconnects for extreme scale computing systems," *Parallel Computing*, vol. 64, pp. 65–80, 2017.

[5] K. Szczerba, T. Lengyel, M. Karlsson, P. A. Andrekson, and A. Larsson, "94-Gb/s 4-PAM using an 850-nm VCSEL, pre-emphasis, and receiver equalization," *IEEE Photonics Technology Letters*, vol. 28, no. 22, pp. 2519–2521, 2016.

[6] M. B. Aziz, S. Giannakopoulos, A. Grabowski, and P. Andrekson, "Word Length Dependent Sensitivity Penalty in High Speed VCSEL-Based Optical Interconnects," *IEEE Photonics Technology Letters*, vol. 36, no. 19, pp. 1181–1184, 2024.

[7] C. Minkenberg, R. Krishnaswamy, A. Zilkie, and D. Nelson, "Co-packaged datacenter optics: Opportunities and challenges," *IET optoelectronics*, vol. 15, no. 2, pp. 77–91, 2021.

[8] E. A. Kadir, R. Shubair, S. K. A. Rahim, M. Himdi, M. R. Kamarudin, and S. L. Rosa, "B5G and 6G: Next generation wireless communications technologies, demand and challenges," in *2021*

*International Congress of Advanced Technology and Engineering (ICOTEN)*. IEEE, 2021, pp. 1–6.

[9] W. Jian-quan, M. Zhang-chao, S. Lei, Z. Chao-yi, and L. Wei, "Evolution, key technology, prospects, and applications of industrial network architecture," *Chinese Journal of Engineering*, vol. 45, no. 8, pp. 1376–1389, 2023.

[10] E. Simpanen, "1060 nm GaAs VCSELs for Extended Reach Optical Interconnects in Data Centers," Ph.D. dissertation, Department of Microtechnology and Nanoscience, Chalmers University of Technology, 2018.

[11] L. Lo Bello, G. Patti, and L. Leonardi, "A perspective on ethernet in automotive communications—Current status and future trends," *Applied Sciences*, vol. 13, no. 3, p. 1278, 2023.

[12] I. E. book. (2023) Ethernet celebrates 50 years with 2023 roadmap and demo. Accessed: 2024-11-20.

[13] W. Tian, H. Hou, H. Dang, X. Cao, D. Li, S. Chen, and B. Ma, "Progress in Research on Co-Packaged Optics," *Micromachines*, vol. 15, no. 10, p. 1211, 2024.

[14] M.-J. Lu, S.-Y. Mu, C.-S. Cheng, and J. Chen, "Advanced packaging technologies for copackaged optics," in *2022 IEEE 72nd Electronic Components and Technology Conference (ECTC)*. IEEE, 2022, pp. 38–42.

[15] Broadcom. (2024) What is 6G Technology, How Fast Will it be, and When is it Rolling Out? Accessed: 2024-11-11.

[16] C. E. Shannon, "A mathematical theory of communication," *The Bell system technical journal*, vol. 27, no. 3, pp. 379–423, 1948.

[17] C. E. Shannon, "Communication in the presence of noise," *Proceedings of the IRE*, vol. 37, no. 1, pp. 10–21, 1949.

[18] Q. Hu, D. Che, Y. Wang, and W. Shieh, "Advanced modulation formats for high-performance short-reach optical interconnects," *Optics express*, vol. 23, no. 3, pp. 3245–3259, 2015.

[19] X. Pang, O. Ozolins, R. Lin, L. Zhang, A. Udalcovs, L. Xue, R. Schatz, U. Westergren, S. Xiao, W. Hu *et al.*, "200 Gbps/lane IM/DD technologies for short reach optical interconnects," *Journal of Lightwave Technology*, vol. 38, no. 2, pp. 492–503, 2020.

[20] D. Tonietto, "The future of short reach interconnect," in *ESSCIRC 2022-IEEE 48th European Solid State Circuits Conference (ESSCIRC)*. IEEE, 2022, pp. 1–8.

[21] Y. Matsui, "Directly modulated laser technology: Past, present, and future," in *Datacenter Connectivity Technologies*. River Publishers, 2022, pp. 87–171.

[22] P. Pepeljugoski, S. E. Golowich, A. J. Ritger, P. Kolesar, and A. Risteski, "Modeling and simulation of next-generation multimode fiber links," *Journal of Lightwave Technology*, vol. 21, no. 5, p. 1242, 2003.

[23] D. Gloge, "Optical power flow in multimode fibers," *Bell System Technical Journal*, vol. 51, no. 8, pp. 1767–1783, 1972.

[24] J. Carpenter and T. D. Wilkinson, "Characterization of multimode fiber by selective mode excitation," *Journal of lightwave technology*, vol. 30, no. 10, pp. 1386–1392, 2012.

[25] L. G. Wright, Z. M. Ziegler, P. M. Lushnikov, Z. Zhu, M. A. Eftekhar, D. N. Christodoulides, and F. W. Wise, "Multimode nonlinear fiber optics: massively parallel numerical solver, tutorial, and outlook," *IEEE Journal of Selected Topics in Quantum Electronics*, vol. 24, no. 3, pp. 1–16, 2017.

[26] R. Olshansky and D. B. Keck, "Pulse broadening in graded-index optical fibers," *Applied Optics*, vol. 15, no. 2, pp. 483–491, 1976.

[27] G. Yabre, "Comprehensive theory of dispersion in graded-index optical fibers," *Journal of lightwave technology*, vol. 18, no. 2, p. 166, 2000.

[28] Y. Sun and J. Kamino, "Optical Fiber for Datacenter Connectivity," in *Datacenter Connectivity Technologies*. River Publishers, 2022, pp. 213–277.

[29] M.-J. Li, X. Chen, A. R. Zakharian, J. E. Hurley, and J. S. Stone, "Large core multimode Fiber for short distance communications," in *2022 27th OptoElectronics and Communications Conference (OECC) and 2022 International Conference on Photonics in Switching and Computing (PSC)*. IEEE, 2022, pp. 1–3.

[30] L. Chrostowski and K. Iniewski, *High-speed photonics interconnects*. CRC Press, 2017.

[31] R. Michalzik, "VCSEL fundamentals," in *VCSELs: fundamentals, technology and applications of vertical-cavity surface-emitting lasers*. Springer, 2012, pp. 19–75.

[32] P. Moser and P. Moser, "VCSEL fundamentals," *Energy-Efficient VCSELs for Optical Interconnects*, pp. 13–44, 2016.

[33] L. A. Coldren and E. R. Hegblom, *Fundamental issues in VCSEL design*. Cambridge University Press, 1999.

[34] R. Michalzik and K. J. Ebeling, "Operating principles of VCSELs," in *Vertical-Cavity Surface-Emitting Laser Devices*. Springer, 2003, pp. 53–98.

[35] F. Koyama, "Recent advances of VCSEL photonics," *Journal of Lightwave Technology*, vol. 24, no. 12, pp. 4502–4513, 2006.

[36] B. D. Padullaparthi, J. Tatum, and K. Iga, *VCSEL Industry: Communication and Sensing*. John Wiley & Sons, 2021.

[37] N. N. Ledentsov, O. Y. Makarov, V. A. Shchukin, V. Kalosha, N. Ledentsov, L. Chrochos, M. B. Sanayeh, and J. P. Turkiewicz, "High speed VCSEL technology and applications," *Journal of Lightwave Technology*, vol. 40, no. 6, pp. 1749–1763, 2022.

[38] J.-F. P. Seurin, "High-power VCSEL arrays," in *VCSELs: Fundamentals, Technology and Applications of Vertical-Cavity Surface-Emitting Lasers*. Springer, 2012, pp. 263–290.

[39] R. Michalzik, "A New VCSEL Book," *Institute of Optoelectronics*, p. 77.

[40] S. B. Healy, E. P. O'Reilly, J. S. Gustavsson, P. Westbergh, Å. Haglund, A. Larsson, and A. Joel, "Active region design for

high-speed 850-nm VCSELs," *IEEE Journal of Quantum Electronics*, vol. 46, no. 4, pp. 506–512, 2010.

[41] C. W. Wilmsen, H. Temkin, and L. A. Coldren, *Vertical-cavity surface-emitting lasers: design, fabrication, characterization, and applications*. Cambridge University Press, 2001, vol. 24.

[42] S. Wu and H. Weng, "17 Semiconductor Lasers," *Handbook of Semiconductors: Fundamentals to Emerging Applications*, p. 222, 2024.

[43] Y. Ou, J. S. Gustavsson, P. Westbergh, A. Haglund, A. Larsson, and A. Joel, "Impedance characteristics and parasitic speed limitations of high-speed 850-nm VCSELs," *IEEE Photonics Technology Letters*, vol. 21, no. 24, pp. 1840–1842, 2009.

[44] G. P. Agrawal, *Fiber-optic communication systems*. John Wiley & Sons, 2012.

[45] W. Nakwaski, "Thermal aspects of efficient operation of vertical-cavity surface-emitting lasers," *Optical and Quantum Electronics*, vol. 28, pp. 335–352, 1996.

[46] P. Westbergh, J. S. Gustavsson, Å. Haglund, M. Skold, A. Joel, and A. Larsson, "High-speed, low-current-density 850 nm VCSELs," *IEEE Journal of Selected Topics in Quantum Electronics*, vol. 15, no. 3, pp. 694–703, 2009.

[47] Y.-C. Chang and L. A. Coldren, "Design and performance of high-speed VCSELs," in *VCSELs: Fundamentals, Technology and Applications of Vertical-Cavity Surface-Emitting Lasers*. Springer, 2012, pp. 233–262.

[48] S. Wu and H. Weng, "Semiconductor Lasers," in *Handbook of Semiconductors*. CRC Press, pp. 222–234.

[49] K. J. Ebeling, "Analysis of vertical cavity surface emitting laser diodes (VCSEL)," in *Semiconductor Quantum Optoelectronics*. CRC Press, 2020, pp. 295–338.

[50] H.-J. Zepernick and A. Finger, *Pseudo random signal processing: theory and application*. John Wiley & Sons, 2013.

[51] L. Blum, M. Blum, and M. Shub, "A simple unpredictable pseudo-random number generator," *SIAM Journal on computing*, vol. 15, no. 2, pp. 364–383, 1986.

[52] M. Müller, "Fundamentals of Digital Communications Systems."

[53] K. Zhu and V. Saxena, "From design to test: A high-speed PRBS," *IEEE Transactions on Very Large Scale Integration (VLSI) Systems*, vol. 26, no. 10, pp. 2099–2107, 2018.

[54] Y. Zhu, Y. Li, D. Li, L. Dong, X. Liu, A. Yan, Y. Liu, and Z. Wang, "A Theoretical and Experimental Analysis of the Time-Domain Characteristics of a PRBS Phase-Modulated Laser System," *Applied Sciences*, vol. 14, no. 20, p. 9198, 2024.

[55] E. P. Haglund, P. Westbergh, J. S. Gustavsson, and A. Larsson, "Impact of damping on high-speed large signal VCSEL dynamics," *Journal of Lightwave Technology*, vol. 33, no. 4, pp. 795–801, 2014.

[56] A. Grabowski, J. Gustavsson, Z. S. He, and A. Larsson, "Large-signal equivalent circuit for datacom VCSELs," *Journal of Lightwave Technology*, vol. 39, no. 10, pp. 3225–3236, 2021.

[57] W. Hamad, M. B. Sanayeh, T. Siepelmeyer, H. Hamad, and W. H. Hofmann, "Small-signal analysis of high-performance VCSELs," *IEEE Photonics Journal*, vol. 11, no. 2, pp. 1–12, 2019.

[58] Y. Rao, W. Yang, C. Chase, M. C. Huang, D. P. Worland, S. Khaleghi, M. R. Chitgarha, M. Ziyadi, A. E. Willner, and C. J. Chang-Hasnain, "Long-wavelength VCSEL using high-contrast grating," *IEEE Journal of Selected Topics in Quantum Electronics*, vol. 19, no. 4, pp. 1 701 311–1 701 311, 2013.

[59] "Energy efficiency of VCSELs in the context of short-range optical links, author=Szczerba, Krzysztof and Westbergh, Petter and Gustavsson, Johan S and Karlsson, Magnus and Andrekson, Peter A and Larsson, Anders," *IEEE Photonics Technology Letters*, vol. 27, no. 16, pp. 1749–1752, 2015.

[60] G. Breed, "Bit error rate: Fundamental concepts and measurement issues," *High Frequency Electronics*, vol. 2, no. 1, pp. 46–47, 2003.

[61] M. Jeruchim, "Techniques for estimating the bit error rate in the simulation of digital communication systems," *IEEE Journal on selected areas in communications*, vol. 2, no. 1, pp. 153–170, 1984.

[62] H. M. Gach, I. J. Lowe, D. P. Madio, A. Caprihan, S. A. Altobelli, D. O. Kuethe, and E. Fukushima, "A programmable pre-emphasis system," *Magnetic resonance in medicine*, vol. 40, no. 3, pp. 427–431, 1998.

[63] A. Nafaa, T. Taleb, and L. Murphy, "Forward error correction strategies for media streaming over wireless networks," *IEEE Communications Magazine*, vol. 46, no. 1, pp. 72–79, 2008.

[64] M. Forbes, J. Gourlay, and M. Desmulliez, "Optically interconnected electronic chips: a tutorial and review of the technology," *Electronics & Communication Engineering Journal*, vol. 13, no. 5, pp. 221–232, 2001.

[65] H.-T. Cheng, Y.-C. Yang, T.-H. Liu, and C.-H. Wu, "Recent advances in 850 nm VCSELs for high-speed interconnects," in *Photonics*, vol. 9, no. 2. MDPI, 2022, p. 107.

[66] K. Iga, T. Kambayashi, and C. Kitahara, "Surface-emitting GaInAsP/InP laser (I)," in *Proceedings of the 25th Joint Conference on Applied Physics, Tokyo, Japan*, 1978, p. 63.

[67] H. Soda, K.-i. Iga, C. Kitahara, and Y. Suematsu, "GaInAsP/InP surface emitting injection lasers," *Japanese Journal of Applied Physics*, vol. 18, no. 12, p. 2329, 1979.

[68] K. Iga, F. Koyama, and S. Kinoshita, "Surface emitting semiconductor lasers," *IEEE Journal of Quantum Electronics*, vol. 24, no. 9, pp. 1845–1855, 1988.

[69] "IEEE Standard for Information technology - Local and metropolitan area networks - Part 3: CSMA/CD Access Method and Physical Layer Specifications - Media Access Control (MAC) Parameters, Physical Layer, and Management Parameters for 10 Gb/s Operation," *IEEE Std 802.3ae-2002 (Amendment to IEEE Std 802.3-2002)*, pp. 1–544, 2002.

[70] P. L. Specifications, "Management Parameters for 40 Gb/s and 100 Gb/s Operation over Fiber Optic Cables," *IEEE Standard for Ethernet*.

[71] "IEEE Standard for Ethernet - Amendment 10: Media Access Control Parameters, Physical Layers, and Management Parameters for 200 Gb/s and 400 Gb/s Operation," *IEEE Std 802.3bs-2017 (Amendment to IEEE 802.3-2015 as amended by IEEE's 802.3bw-2015, 802.3by-2016, 802.3bq-2016, 802.3bp-2016, 802.3br-2016, 802.3bn-2016, 802.3bz-2016, 802.3bu-2016, 802.3bv-2017, and IEEE 802.3-2015/Cor1-2017)*, pp. 1–372, 2017.

[72] "IEEE Standard for Ethernet – Amendment 7: Physical Layer and Management Parameters for 400 Gb/s over Multimode Fiber," *IEEE Std 802.3cm-2020 (Amendment to IEEE Std 802.3-2018 as amended by IEEE Std 802.3cb-2018, IEEE Std 802.3bt-2018, IEEE Std 802.3cd-2018, IEEE Std 802.3cn-2019, IEEE Std 802.3cg-2019, and IEEE Std 802.3cq-2020)*, pp. 1–72, 2020.

[73] A. Richter, S. Dris, I. Koltchanov, S. Alreesh, D. Yevseyenko, and E. Sokolov, "Optical interconnects for datacenter links: Design and modeling challenges," in *Optical Interconnects XX*, vol. 11286. SPIE, 2020, pp. 241–251.

[74] D. M. Kuchta, P. Pepeljugoski, and Y. Kwark, "VCSEL modulation at 20 Gb/s over 200 m of multimode fiber using a 3.3 V SiGe laser driver IC," in *2001 Digest of LEOS Summer Topical Meetings: Advanced Semiconductor Lasers and Applications/Ultraviolet and Blue Lasers and Their Applications/Ultralong Haul DWDM Transmission and Networking/WDM Compo.* IEEE, 2001, pp. 2–pp.

[75] N. Nishiyama, M. Arai, S. Shinada, K. Suzuki, F. Koyama, and K. Iga, "Multi-oxide layer structure for single-mode operation in vertical-cavity surface-emitting lasers," *IEEE Photonics Technology Letters*, vol. 12, no. 6, pp. 606–608, 2000.

[76] M. Azuchi, N. Jikutani, M. Arai, T. Kondo, and F. Koyama, "Multioxide layer vertical-cavity surface-emitting lasers with improved modulation bandwidth," in *CLEO/Pacific Rim 2003. The 5th Pacific Rim Conference on Lasers and Electro-Optics (IEEE Cat. No. 03TH8671)*, vol. 1. IEEE, 2003, pp. 163–Vol.

[77] P. Westbergh, J. S. Gustavsson, B. Kögel, Å. Haglund, A. Larsson, A. Mutig, A. Nadtochiy, D. Bimberg, and A. Joel, "40 Gbit/s error-free operation of oxide-confined 850 nm VCSEL," *Electronics Letters*, vol. 46, no. 14, p. 1, 2010.

[78] P. Westbergh, R. Safaisini, E. Haglund, J. S. Gustavsson, A. Larsson, and A. Joel, "High-speed 850-nm VCSELs with 28 GHz modulation bandwidth for short reach communication," in *Vertical-Cavity Surface-Emitting Lasers XVII*, vol. 8639. SPIE, 2013, pp. 251–256.

[79] P. Moser, J. A. Lott, and D. Bimberg, "Energy efficiency of directly modulated oxide-confined high bit rate 850-nm VCSELs for optical interconnects," *IEEE Journal of Selected Topics in Quantum Electronics*, vol. 19, no. 4, pp. 1 702 212–1 702 212, 2013.

[80] E. Haglund, P. Westbergh, J. S. Gustavsson, E. P. Haglund, A. Larsson, M. Geen, and A. Joel, "30 GHz bandwidth 850 nm VCSEL with sub-100 fJ/bit energy dissipation at 25–50 Gbit/s," *Electronics Letters*, vol. 51, no. 14, pp. 1096–1098, 2015.

[81] D. M. Kuchta, A. V. Rylyakov, F. E. Doany, C. L. Schow, J. E. Proesel, C. W. Baks, P. Westbergh, J. S. Gustavsson, and A. Larsson, "A 71-Gb/s NRZ modulated 850-nm VCSEL-based optical link," *IEEE Photonics Technology Letters*, vol. 27, no. 6, pp. 577–580, 2015.

[82] T.-Y. Huang, J. Qiu, C.-H. Wu, H.-T. Cheng, M. Feng, H.-C. Kuo, and C.-H. Wu, "A NRZ-OOK modulated 850-nm VCSEL with 54 Gb/s error-free data transmission," in *The European Conference on Lasers and Electro-Optics*. Optica Publishing Group, 2019, p. cb_p_22.

[83] Y.-C. Yang, H.-T. Cheng, and C.-H. Wu, "Ultra-fast and Highly Efficient 850-nm VCSELs for Next-gen PAM-4 Transceivers," in *Asia Communications and Photonics Conference*. Optica Publishing Group, 2021, pp. W3D–4.

[84] C. Wang, M. Liu, M. Feng, and N. Holonyak, "Microwave extraction method of radiative recombination and photon lifetimes up to 85° C on 50 Gb/s oxide-vertical cavity surface emitting laser," *Journal of Applied Physics*, vol. 120, no. 22, 2016.

[85] H.-L. Wang, J. Qiu, X. Yu, M. Feng, and N. Holonyak, "85° C operation of 850 nm VCSELs deliver a 42 Gb/s error-free data transmission for 100 meter MMF link," in *Optical Fiber Communication Conference*. Optica Publishing Group, 2018, pp. W1I–6.

[86] H.-L. Wang, W. Fu, J. Qiu, and M. Feng, "850 nm VCSELs for 50 Gb/s NRZ Error-Free Transmission over 100-meter OM4 and

up to 115 C Operation," in *2019 Optical Fiber Communications Conference and Exhibition (OFC)*. IEEE, 2019, pp. 1–3.

[87] N. Ledentsov Jr, M. Agustin, V. A. Shchukin, J.-R. Kropp, N. N. Ledentsov, J. Turkiewicz, Z. Khan, C.-L. Cheng, J. Shi, N. Cherkashin *et al.*, "Quantum dot 850 nm VCSELs with extreme high temperature stability operating at bit rates up to 25 Gbit/s at 150° C," *Solid-State Electronics*, vol. 155, pp. 150–158, 2019.

[88] N. Ledentsov, L. Chorchos, O. Makarov, J.-R. Kropp, V. A. Shchukin, V. Kalosha, J. P. Turkiewicz, N. Cherkashin, and N. N. Ledentsov, "Quantum-dot oxide-confined 850-nm VCSELs with extreme temperature stability operating at 25 Gbit/s up to 180deg C," in *Vertical-Cavity Surface-Emitting Lasers XXIV*, vol. 11300. SPIE, 2020, pp. 90–96.

# Included papers A-B

# Paper A

M. Bilal Aziz, Stavros Giannakopoulos, Alexander Grabowski, Peter Andrekson, "Word Length Dependent Sensitivity Penalty in High Speed VCSEL-Based Optical Interconnects", *Photonics Technology Letters*, 36, Issue: 19, 1181 - 1184, 2024.

# Paper B

M. Bilal Aziz, Hans Daniel Kaimre, Peter Andrekson, "High-Speed Transmission of 850 nm VCSEL Optical Interconnects Across Wide Temperatures", *Submitted*, 2024.